

RESEARCH PAPER

Design of substrate integrated waveguides based on nanowires: numerical guidelines

Vivien Van Kerckhoven^{1,2} | Luc Piraux¹ | Isabelle Huynen²

¹IMCN Institute, Université catholique de Louvain, 1348 Louvain-la-Neuve, Belgium

²ICTEAM Institute, Université catholique de Louvain, 1348 Louvain-la-Neuve, Belgium

Correspondence

*Isabelle Huynen. Email: isabelle.huynen@uclouvain.be

Present Address

ICTEAM Institute, ELEN division, box L5.03.02, 1348 Louvain-la-Neuve, Belgium

Summary

A thorough study of the parameters influencing the operation of devices based on nanowired alumina substrate is presented. The basic structures are realised by growing metallic nanowires inside alumina porous substrate. The control of the areas wherein growth occurs allows to build various microwave devices supported on the filled template. The performances of these devices depend on the material parameters and topology/geometry in presence. These devices have the particularity to combine nanoscale, through the use of nanowires, and millimeter scale that is characteristic of microwave devices and their associated operating wavelength. The gap between the two-scale ranges implies that analytical models and numerical simulation tools have to be combined to modelize and design performant microwave devices, such as Nanowired Substrate Integrated Waveguides (NSIW) devices that are the subject of the paper. A deep parametric analysis of the properties and operation of the basic NSIW is presented and is followed by the illustration of two designs: a simple NSIW line, and an EBG NSIW filter.

KEYWORDS:

microwaves, nanowires, modelling, design, FEM simulation, Substrate Integrated Waveguide

1 | INTRODUCTION

Nanowires embedded in porous templates have been extensively used to fabricate monolithic planar devices, taking advantage of the interaction between microwave signals and nanowires.

The insertion of nanowires in microwave devices yields various advantages over classical ones: larger range of operational frequencies, better stability over temperature, higher compacity through integration into a single substrate. Compared to classical ferrites, arrays of ferromagnetic nanowires have higher saturation magnetization and ferromagnetic resonance (FMR) and can operate at higher frequencies, due to their large aspect ratio.

Thanks to those properties, noise suppressors⁴, absorbers^{1,2}, inductors³ or filters based on electromagnetic band-gap effect⁵ have been developed, together with non-reciprocal devices, such as phase shifters⁸, isolators⁷ and circulators⁶. More recently slow-wave transmission lines were designed exploiting the high permittivity of metallic nanowire arrays¹⁰, while a filter was designed using the double ferromagnetic resonance effect in magnetic nanowires¹¹. Finally, microstrip and coplanar topologies combining different nanowire materials have been designed.

⁰**Abbreviations:** RW, rectangular waveguide; SIW, Substrate Integrated Waveguide; AAO, Anodized Aluminum Oxide; NW, nanowire; EBG, Electromagnetic Band Gap; MS, Microstrip; FEM, Finite-Element Method; CPWG, Coplanar Waveguide With Ground; RW: Rectangular Waveguide

As outlined in²², high-quality transmission lines are necessary to match the constraints of low cost and consumption, high density, high operational frequency, ... Above 30 GHz, interferences and radiation losses degrade the performances of classical planar topologies such as microstrip and coplanar lines. Hence, the substrate integrated waveguide (SIW) concept¹² is an interesting solution. A rectangular section of shielded line, allowing to reduce radiation, is obtained by drilling two rows of vertical metallic wires or metallized vias throughout the entire height of a substrate. The presence of wires also prevents spurious interferences by crosstalk due to electromagnetic coupling between adjacent devices in a same circuit. Crosstalk as low as -20 dB²⁸, -39 dB³⁰, or even -50 dB²⁹ are reported for SIW technology. Antennas, filters, couplers, power suppliers, can be integrated into the same substrate, for operation up to 180 GHz, and using different kinds of substrates (PCB, paper, polymers or alumina)^{13,14}. In⁵³ an original architecture of hollow SIW was proposed, allowing to reduce insertion losses. On the other hand, a review and recent developments on SIW antennas can be found in^{31,32,33}. In⁵² an architecture dual to nanowire-based EBG is proposed; the contrast in dielectric constant inducing the bandgap is created by drilling holes in perioding areas of a dielectric substrate; the air filling the holes contrasts with the dielectric constant of the substrate.

Taking into account the respective advantages of nanowires and Substrate Integrated Waveguide (SIW) devices^{15,16,22}, their combination is a promising approach. Indeed metallic nanowire arrays are deposited in a porous alumina template to form the waveguide walls. Then, Cu layers deposited on the top and bottom surfaces of the alumina substrate form a simple rectangular waveguide (RW). Competitive devices can be obtained by inserting in the waveguide cavity various nanowire arrays, combining different heights, shapes and materials (magnetic or not). Their fabrication requires the growth of nanowires inside the template in dedicated locations with good precision and accuracy. In³⁹ we compared two different laser processes set up for the precise positioning of areas hosting the growth of nanowires in a porous alumina membrane.

In this paper, we present a detailed numerical study that can serve as guidelines for the design of novel microwave devices based on nanoporous templates. A parametric analysis is performed involving various parameters affecting the operation and performances of the so-called Nanowired Substrate Integrated (NSIW) devices. Due to the two-scale ranges in presence, nano- and millimeter, analytical simulations are combined with FEM simulations using the COMSOL software. The established guidelines are applied as an example of the design of two NSIW devices.

2 | THE NANOWIRED SUBSTRATE INTEGRATED WAVEGUIDE (NSIW)

Figure 1 shows a schematic of the porous template supporting the Nanowired Substrate Integrated Waveguide. Some regions of the alumina template are filled through electrodeposition of nanowire arrays. The procedure of electrodeposition described in¹⁸ allows fine control of the height of deposited nanowires (NWs), while their diameter is fixed by the pore diameter of the membrane, shown in Figure 2.

The porous templates used for this work are anodized aluminium oxide (AAO) membranes from Smart Membranes GmbH (Figure 2). The pore diameter is 40 nm, the distance between pores is 125 nm, and the thickness is 100 μm .

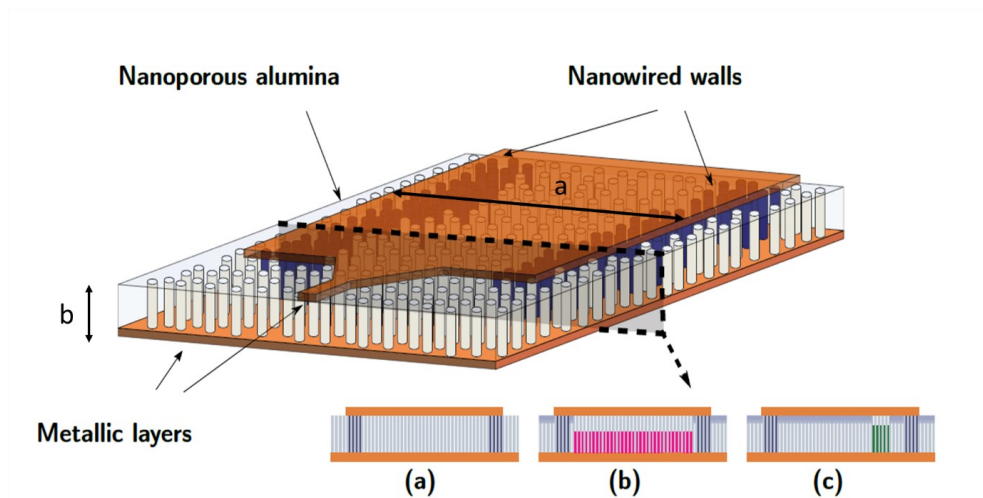


FIGURE 1 Schematic view of the NSIW in the alumina template, and different possible profile sections: (a) empty waveguide (b) homogeneous filling (c) asymmetric filling used for the isolator device³⁹.

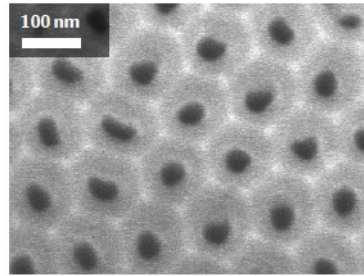


FIGURE 2 SEM images of a self-supported AAO templates with a pore diameter of 40 nm, an interpore distance of 125 nm, and a thickness of 100 μm .

In order to form the NSIW, two parallel rows of nanowire arrays separated by a distance a are electro-deposited into the nanoporous template. Next, the template is covered on both faces by 3 μm thick copper layer (see Figure 1). The result is a shielded rectangular waveguide having metallic walls formed by the rows of nanowires, and through which precise modes of the signal defined by the classical RW theory¹⁷ can propagate. As will be explained in Section 3.3, modes can only propagate above a cut-off frequency f_c which depends on the width a and height b of the NSIW, on the medium relative permittivity and permeability and on the type of mode propagating in the NSIW.

The NSIW has the following advantages:

- **Size and compactness.** One of the main advantages of the NSIW is related to its size. All the components of a device are embedded inside an AAO membrane which thickness is about 100 μm . Moreover, as explained in^{6,7,8,15,16}, no magnets are required to produce non-reciprocal effects. These magnets significantly increase the size of the devices. For the purpose of miniaturization, it is therefore interesting to dispense with them.
- **Tunable permittivity and permeability.** The ability to insert additional nanowire arrays in the waveguide cavity is also a strong potentiality of this technique as it allows to tune precisely the permittivity and permeability of the substrate. The effective permittivity of a metallic nanowire array is directly related to its height while the permeability of a magnetic array is also related to its constitutive material.
- **Low losses.** Given the architecture of the NSIW, low losses rates are expected. Radiation losses should be almost zero: given the density of the wires constituting the vertical walls, no leakage should pass through. However, the substrates used are usually very thin such that conductive losses could become important.

The following sections are dedicated to the theoretical analysis of the assertions mentioned above. Applying the theory of rectangular waveguide (RW), SIW and NWS, we will try to confirm or invalidate the expected properties of nanowires combined with SIW. The influence of the following factors on the performances of the NSIW will be investigated:

- width of the NSIW
- nanowired walls
- modes of propagation
- effective medium filling the NSIW
- geometry of the transitions
- losses

All these parameters are involved in the operation of the NSIW shown in Figure 1. The main parameters considered throughout this study are reported in Table 1.

TABLE 1 Values of the geometrical and physical parameters considered in this study.

Parameter	Notation	Value
Width of NSIW	a	6 mm
Height of NSIW = height of AAO template	b	100 μm
Pore diameter of AAO	d	40 nm
Interpore distance of AAO	s	125 nm
Dielectric constant of alumina Al_2O_3	ϵ_r	9.8
Loss tangent factor of Al_2O_3	$\tan \delta$	1.5×10^{-2}
Permeability of Al_2O_3	μ_r	1
Operational frequency	f_0	12.5 GHz or 25 GHz

3 | PARAMETRIC ANALYSIS

3.1 | Waveguide width

The most important dimension of a waveguide is its width: the distance a between the two vertical vias rows. This width determines directly the cut-off frequency (see Section 3.3) and influences the evolution of the propagation beyond the cut-off. We will see how to determine the width a that an NSIW device should have if this device is aimed to work around an operational frequency f_0 . Given the particularities of the NSIW, different approaches will be explored.

One of the objectives of the SIW geometry is to reproduce the characteristic propagation modes of the rectangular waveguide (RW) inside a thin template. In the typical SIW geometry, a is the distance between the two vias rows from center-to-center (see Figure 1). Due to the vias geometry, this distance cannot be utilized directly in the same way as for the classical RW. Indeed, because of the distance between the successive vias and because of their circular shape, the signal inside the guide does not behave exactly like in a perfect RW whose width is also a . To apply the RW theory to the SIW, an effective width can be used. It has to take into account the shape of the vias and the space s in-between. Obviously, its value has to be between $a - d$ and $a + d$. Its common definition is given by equation (1) provided in^{41,42}

$$a_{\text{eff}} = a - \frac{d^2}{0.95 s} \quad (1)$$

Using this effective width, the propagation constant of a SIW will be similar to that of a classical RW whose width is a_{eff} .

In the case of nanowire-based devices, the vias diameter is the diameter of the template nanopores and their longitudinal spacing is the interpore distance. If a is the center-to-center distance between the two closest rows of nanowires, the effective width can be determined from the morphological characteristics of the template (see Table 1). Since the distance a is in the order of few millimetres, the width and the effective width are almost equal. Indeed, in the case of 100 μm -thick membrane, we obtain from equation (2) and the data of Table 1 :

$$a_{\text{eff}} = a - \frac{(40 \text{ nm})^2}{0.95 \times 125 \text{ nm}} = a - 13.97 \text{ nm} \approx a \quad (2)$$

since, as will be verified later, the width a of the designed NSIW is in the millimetric range.

3.2 | Nanowired walls

The two vertical walls of the NSIW are made with metallic nanowires electrodeposited in the nanoporous alumina. The purpose of these walls is to ensure a proper electrical connection between the two horizontal metallic conductors to induce cancellation of the electric field tangential to the vertical walls, as in a classical microwave metallic RW. Thus, they must be constituted of good electrical conductors. If the wall conductivity is not good enough, some conductive losses will emerge as will be seen in Section 3.6. If they are not thick enough, some radiation losses will appear: the electric field will not cancel in the wall and will radiate outside of the waveguide. On the other hand, we could use unnecessary space by making these walls too wide. An intermediate value must therefore be estimated. Since reducing the volume of microwave devices is always interesting, we will look for the minimal value of the wall thickness. For that purpose, it is appropriate to use the concept of skin depth. If an electric current flows with an angular frequency ω through a conductor having a permeability μ and a conductivity σ , the skin depth δ is defined by equation (3)

$$\delta = \sqrt{\frac{2}{\omega \mu \sigma}} \quad (3)$$

such that the attenuation of the EM fields through the conductor depth will be described by $e^{-x/\delta}$ where $x = 0$ is located on the surface of the conductor. Over a length of one skin depth, the attenuation of the amplitude of the field inside the conductor will be $e^{-1} = 1/e = 36\%$. To block properly an incident signal, the thickness of a conductor must be at least equal to five times the skin depth of this signal passing through. Such a layer will guarantee a field attenuation higher than 95 %. The skin depth of a microwave signal through nanowire arrays has to be determined. The conductivity is dominated by the contribution of the wires and will evolve linearly with the packing factor p of the wires: the larger the density of nanowires in a given section, the more metal will be present in that area and the better its conductivity. This is equivalent to consider that the walls of the NSIW are made of a homogeneous material whose conductivity is given by $p\sigma$, applying a usual volumetric law. The skin depth of this homogeneous material is given by equation (4)

$$\delta = \sqrt{\frac{2}{\omega\mu p\sigma}} \quad (4)$$

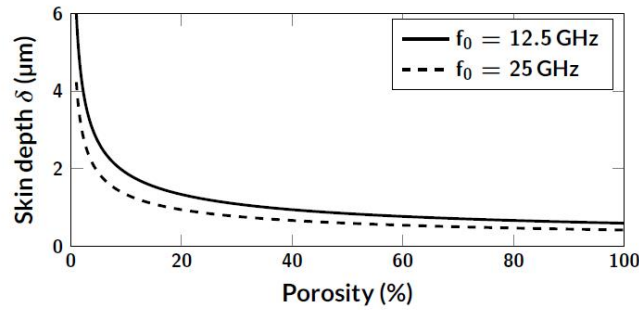


FIGURE 3 Skin depth according to Equation (4) as a function of porosity p of AAO template and for two different operation frequencies f_0 .

Figure 3 shows the skin depth calculated using (4) for Copper nanowires and for the two operating frequencies considered in this work. Considering the porosity of the AAO template used in this work, i.e p around 10 %, it can be concluded that the thickness of the walls of the NSIW has to be superior to $5 \times 2 = 10 \mu\text{m}$ to act as efficient shielding wall for the equivalent RW. It is worth mentioning that it is sufficient for us to verify that the walls of the NSIW act as real shields for it. Also, the diameter of our nanowires is 100 nm. For this value the current distribution in a single nanowire is almost uniform as can be obtained using the formalism discussed in our previous publication¹⁰; the variation is less than 10% if the diameter is less or equal to 100 nm and it has thus no significant influence on the operation of our NSIW devices.

3.3 | Modes of propagation

An interesting approach to determine the optimal waveguide width a is to adjust it to the chosen operational frequency f_0 . Two criteria must be taken into account to operate this optimization.

First, only the dominant mode TE_{10} should be able to propagate through the waveguide at the operational frequency f_0 . The second propagation mode TE_{20} and the followings must not appear because they may create interferences, disturb the propagation and degrade it. The waveguide must therefore be designed so that the operating frequency is sufficiently below the cut-off frequency of the second mode f_{c20} to avoid its appearance.

Secondly, for an efficient use of a transmission line, it is necessary to use it at frequencies where the line is non-dispersive: the phase velocity must be independent of the frequency. This ensures that the signal is not distorted during its propagation because all frequencies will travel along the line at the same speed. This condition is met if the imaginary part β of the propagation constant $\gamma = \alpha + j\beta$ changes linearly with the frequency and if the real part α is independent of it. The phase velocity is given by equation (5)

$$v_p = \frac{\omega}{\beta} = \frac{2\pi f}{\beta} \quad (5)$$

We observe that if β depends linearly on f , v_p will be independent of it. A non-dispersive transmission is also characterized by α independent of f . The attenuation will be identical at all the frequencies: a signal that contains more than one frequency component will not be distorted¹⁷. We can check easily if this condition is respected in the NSIW. For any TE_{mn} mode propagating in a RW, the propagation constant given by equation (6)

$$\gamma = \sqrt{\left(\frac{m\pi}{a}\right)^2 + \left(\frac{n\pi}{b}\right)^2 - \omega^2\mu\epsilon} \quad (6)$$

with attenuation and propagation constant given by expressions (7)

$$\alpha = \Re(\gamma) \quad (7a)$$

$$\beta = \Im(\gamma) \quad (7b)$$

Each TE_{mn} mode propagates when $\beta > 0$, i.e above a cut-off frequency noted f_{cmn} given by expression (8)

$$f_{cmn} = \frac{1}{2\pi\sqrt{\mu\varepsilon}} \sqrt{\left(\frac{m\pi}{a}\right)^2 + \left(\frac{n\pi}{b}\right)^2} \quad (8)$$

For the NSIW topology of Figure 1, representing typical devices under scope, owing to the low thickness of the alumina template $b \ll a$, so that the lowest cut-off frequencies will be f_{c10} , f_{c20} and f_{c30} . Below these frequencies, no propagation of the considered mode occurs ($\beta = 0$), it is attenuated ($\alpha > 0$). Figure 4 shows the evolution of α and β with f for the TE_{10} mode and two values of width a . It is obvious that β will only evolve linearly with $f = \omega/2\pi$ far enough from the cut-off and that α is independent of f in the same frequency range.

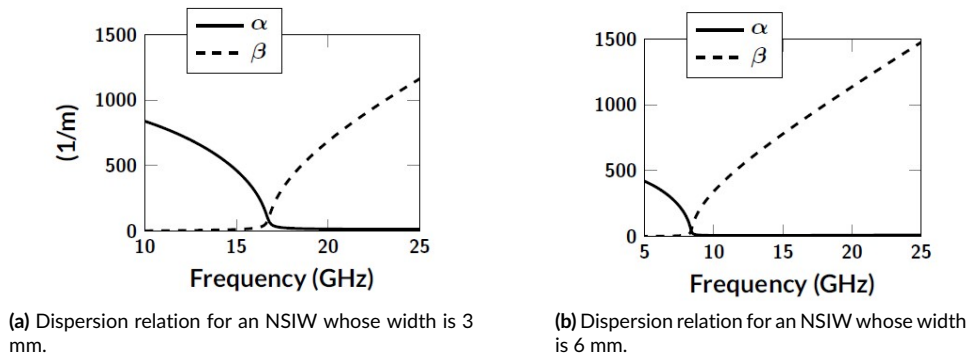


FIGURE 4 Dispersion relation of the NSIW integrated into a nanoporous alumina membrane whose properties are given in Table 1.

The operational frequency must be sufficiently higher than the cut-off frequency f_{c10} in order to induce non-dispersive propagation, and relatively below the cut-off frequency of the second mode f_{c20} to avoid the appearance of this mode. Therefore, we assume that f_0 must be in the middle of this interval, which allows us to write the rule (9):

$$f_0 = \frac{f_{c10} + f_{c20}}{2} = \frac{1}{4\pi\sqrt{\mu\varepsilon}} \left(\frac{\pi}{a} + \frac{2\pi}{a} \right) \quad (9)$$

where a is the width of the NSIW, $\mu = \mu_r\mu_0$ is the permeability and $\varepsilon = \varepsilon_r\varepsilon_0$, with ε_0 the permittivity of vacuum.

There is therefore a direct link between the frequency of use f_0 and the width of the waveguide. The optimal width a as a function of the operational frequency f_0 is given in Figure 5 for an NSIW embedded into a nanoporous alumina membrane. In particular, if the operating frequency f_0 is set at 25 GHz, the optimal width is 3 mm. Similarly, if $f_0 = 12.5$ GHz, we find $a = 6$ mm.

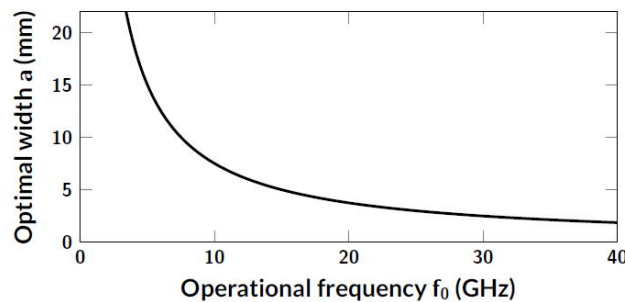


FIGURE 5 Optimal width of an NSIW in a nanoporous alumina membrane whose properties are given in Table 1 (Smart Membranes type). There is no variation induced on a by the height b of the membrane. If the operational frequency f_0 is set to 12.5 GHz, the optimal width will be 6 mm.

3.4 | Effective medium filling the NSIW

In an NSIW, the inner medium is neither homogeneous nor isotropic. A material is homogeneous if it has the same properties everywhere. In porous alumina, the air-filled pores are not electrically identical to the bulk alumina situated in-between. Likewise, porous alumina is not isotropic: it does not have the same properties in all the directions (Figure 6). Because of the vertical pores, the y direction has different properties than the x and z directions. Thus, the permittivity ε_{AAO} of the nanoporous alumina should be a tensor mixture of the permittivities of air and alumina, while the permeability μ is not affected because both relative permeabilities of air and alumina are equal to 1. However, the TE_{mn} modes in a rectangular waveguide have only a component of the electric field oriented along the vertical y axis of the nanowires (Figure 6), and will only interact with the tensor component in this direction. In this direction, the composite medium can be replaced by an effective homogeneous medium because the inclusions have scale lengths much smaller than the wavelength of the EM signal: from the point of view of the fields, the medium is continuous.

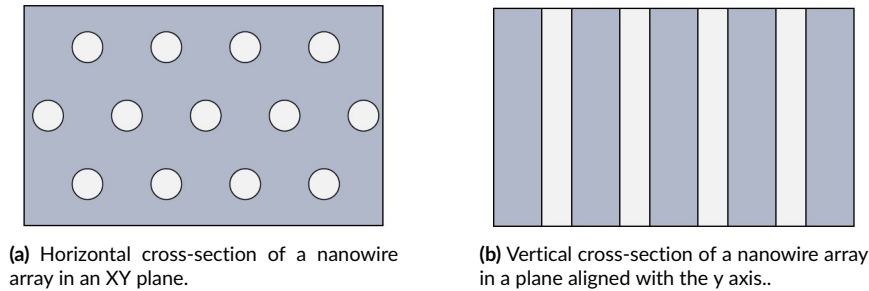


FIGURE 6 Schematic drawings of two cross-sectional views of a nanowire array in a horizontal (a) and vertical (b) directions. Dark grey is for bulk alumina Al_2O_3 . Light color represents empty nanopores aligned with the y axis.

The relative permittivity of nanoporous AAO is hence given by the volumetric law (10)

$$\varepsilon_{r,AAO} = p\varepsilon_{r,air} + (1 - p)\varepsilon_{r,Al_2O_3} \quad (10)$$

with p the porosity of the alumina template, $\varepsilon_{r,air} = 1$ the permittivity of the empty pores, $\varepsilon_{r,Al_2O_3} = \varepsilon_a (1 - j \tan \delta_a)$ the permittivity of bulk alumina, $\varepsilon_a = 9.8$ the dielectric constant of bulk alumina and $\tan \delta_a = 1.5 \times 10^{-2}$ its loss tangent factor, as given in Table 1.

Figures 7a and 7b depict the evolution of the permittivity (10) with respect to the NW volume fraction p . The volume fraction of the NWs corresponds to the porosity of the porous AAO membrane. The real part ε'_r and the imaginary part ε''_r are drawn separately.

Figure 7c gives the evolution with the porosity of the first cut-off frequency f_{c10} obtained for a 6 mm-wide SIW integrated on such substrates. The evolution of the difference between the first f_{c10} and third f_{c30} cut-off frequencies is depicted in Figure 7d.

3.5 | Geometry of the transitions

When designing a microwave device, one has always to be sure that it is matched to its surrounding network: their respective characteristic impedances have to be equal. For practical purpose, the impedance of 50Ω is usually taken as reference for microwave networks. Hence, the point is to find a way to build our NSIW devices so that they have a characteristic impedance of 50Ω in the operational frequency range. All the transmission line topologies are associated with two different impedances: wave impedance Z_w and characteristic impedance Z_c . The first one is a characteristic of a kind of wave (TM, TE, or TEM) but is always defined by the ratio of the fields transverse to the direction of propagation. For TE waves in a RW, Z_w is defined by (11) reported in¹⁷

$$Z_w = \frac{\omega\mu}{\beta} \quad (11)$$

The characteristic impedance Z_c is defined by the ratio of the voltage to the current induced by the traveling wave. In the case of the RW, this definition leads to the relationship (12) reported in¹⁷

$$Z_c = 2 \frac{b}{a} Z_w \quad (12)$$

The evolution of Z_w and Z_c are depicted in Figure 8 for an NSIW whose properties are given in Table 1. The real and imaginary parts have been separated. Of course, a large variation around the cut-off is observed as well as a stabilization above 15 GHz.

We can introduce definition (11) into (12) and replace β with its expression depending on a . This leads to equation (13)

$$z_c = 2 \frac{b}{a} \eta \frac{1}{\sqrt{1 - \left(\frac{\lambda_0}{2a}\right)^2}} \quad (13)$$

where $\lambda_0 = 2\pi/\omega\sqrt{\mu\epsilon}$ is the wavelength of a wave in the considered medium. Then, we can isolate a in the previous expression in order to find equation (14)

$$a_m = \sqrt{\left(\frac{2b\eta}{Z_c}\right)^2 + \left(\frac{\lambda_0}{2}\right)^2} \quad (14)$$

This expression gives the width a_m at which the guide is be matched to Z_c according to the frequency (or wavelength) at which this matching is desired.

However, in the case of the NSIW, b is extremely small: around 100 μm . Then, the first term of the right-hand member of Equation (14) is almost zero and the expression of the width no longer depends on Z_c . At very low height, we obtain expression (15)

$$a_m = \frac{\lambda_0}{2} \quad (15)$$

Figure 9 depicts the evolution of a_m with b as given by Equation (14), for three values of Z_c and at two frequencies. It can be seen that below 100 μm , the desired characteristic impedance no longer influences the value of a_m , which converges to $\lambda_0/2$. However, around this wavelength, a singularity exists in the wave impedance due to the cut-off, as shown in Figure 8. This prevents the use of a waveguide around that frequency. We can conclude that it is not possible to use a waveguide matched to 50 Ω because it will only be matched near the cut-off frequency, i.e. at frequencies that are difficult to exploit.

Therefore the concept of transitions enabling to match the low characteristic impedance of the NSIW to 50 Ω is the most relevant solution. Indeed we don't have a simple and efficient mean of directly exciting the propagation modes in the NSIW, either in a development and characterization context or for possible practical uses in a complete circuit. It is thus necessary to use another type of line to feed the guide. The choice is naturally made for microstrip and coplanar architecture, which easily allow integration on a single substrate. We opted for a tapered transition (Figure 10), going from coplanar to microstrip, then from microstrip to NSIW. This allows a slow transition for the electromagnetic fields, which minimizes losses, reflections, and evanescent modes.

A large numerical study was conducted to optimize the transition from the coplanar pads to the NSIW. A waveguide and its transitions were simulated by the COMSOL software, for a set of different values of the geometric transition parameters. All the concerned parameters are described in Figure 10. It was demonstrated that among all the parameters, only the length and width of the taper play an important role. The geometry of the very short section of a coplanar waveguide having a ground formed by the back metallisation of the alumina substrate, noted CPWG, as well

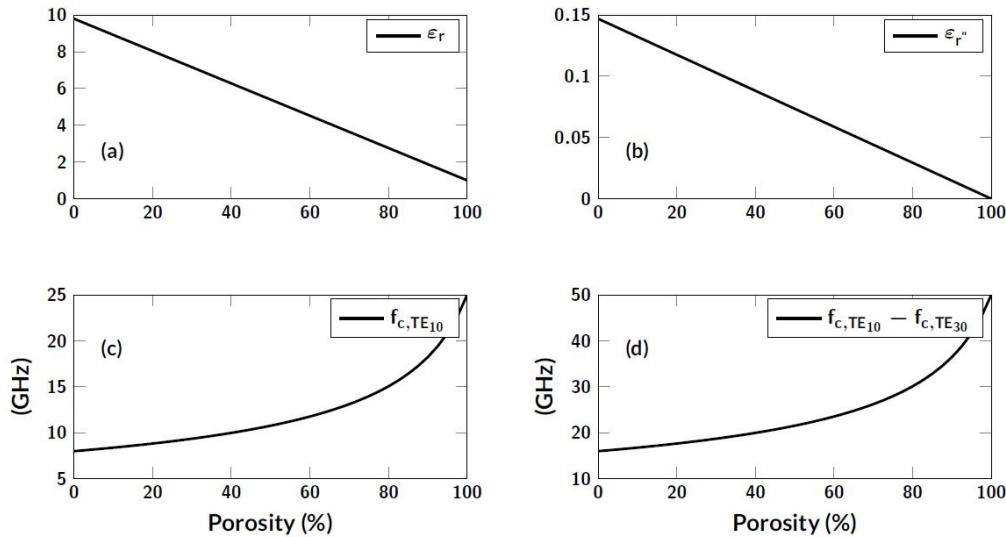


FIGURE 7 Evolution with the substrate porosity of the real part (a) and imaginary part (b) of the effective permittivity given by (10) and Table 1. (c) Evolution with the substrate porosity of the first cut-off frequency $f_{c, TE_{10}}$ for a 6 mm wide NSIW synthesized in a AAO membrane with permittivity given by (10). (d) Evolution with the substrate porosity of the difference between the first $f_{c, TE_{10}}$ and third $f_{c, TE_{30}}$ cut-off frequencies, i.e. $|f_{c, TE_{30}} - f_{c, TE_{10}}|$.

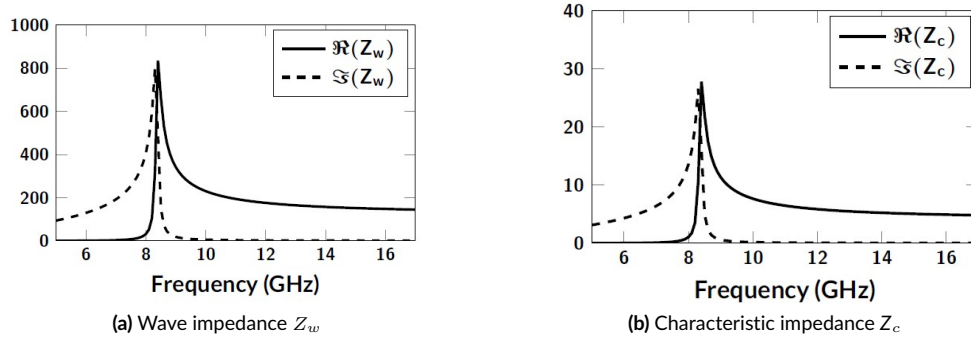


FIGURE 8 Frequency dependence of the wave impedance Z_w (a) and the characteristic impedance Z_c (b) in an NSIW embedded in a porous alumina substrate. The morphological properties of the NSIW are given in Table 1.

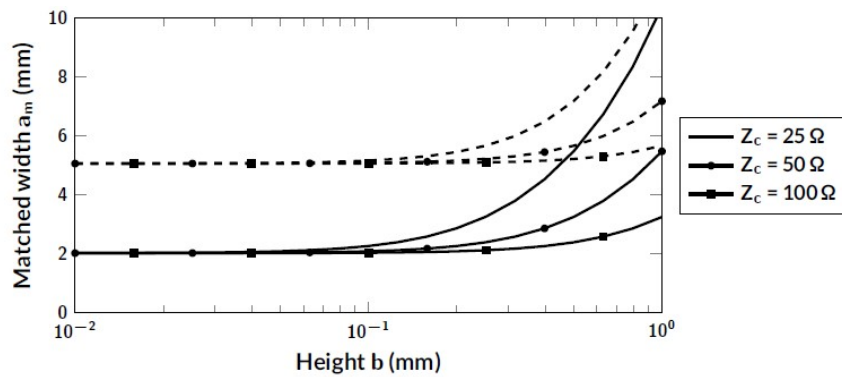


FIGURE 9 Evolution of the waveguide width a_m that will induce a characteristic impedance Z_c with respect to the height of the guide b . This evolution is described by Equation (14). The curves are drawn for three values of Z_c and two frequencies, 25 GHz (solid lines) and 10 GHz (dashed lines).

as the width of the microstrip (MS) line, are determined by the need to be matched to 50Ω . It is interesting to work with taper lengths that are multiples of a quarter wavelength of the signal at the operational frequency of the considered waveguide. Similarly, it is useful to express the taper widths as fractions of the waveguide width. To discriminate between bad and good transitions, different quality parameters have been defined, linked first to the flatness and the mean level of the insertion losses in the dominant mode frequency range, and secondly to the mean level of return losses in the same range. The insertion losses, noted S_{21} , correspond to the ratio of the transmitted signal at the output of the device to the incoming signal. The return losses, noted S_{11} , corresponds to the ratio of the reflected signal at the input of the device by the incoming signal.

With those quality criteria, it appears that the ideal width of a tapered connection between a microstrip line and an NSIW whose width is a is always situated between $0.20 \times a$ and $0.30 \times a$. To optimize the transmission, the length of the taper should be as long as possible. In the simulated range (from 0.1 to 2 times a quarter wavelength), increasing the taper length leads always to better transmission quality. However, after 1, the improvement has no more a crucial impact. Moreover, it increases substantially the size of the device.

A sample of the above results is depicted in Figure 11 for a waveguide whose width is $a = 6$ mm. We observe that the crucial parameter is the width of the tapered transition, while its length has not a lot of influence while longer than a quarter wavelength. The final values resulting from the optimization are given in Table 2.

3.6 | Losses in NSIW

As for all microwave devices, several types of losses may coexist in NSIWs. They are analyzed below.

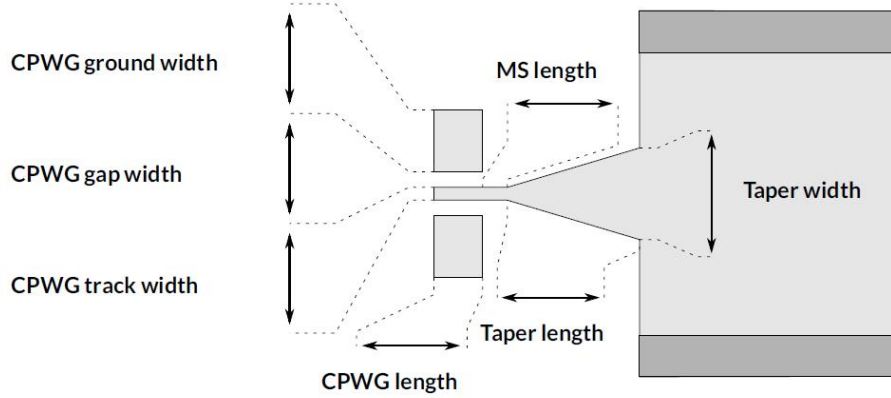


FIGURE 10 Configuration of the transition from coplanar to microstrip and from microstrip to NSIW. The names of all the optimised parameters given correspond to Table 2. The two main parameters are the length and width of the taper.

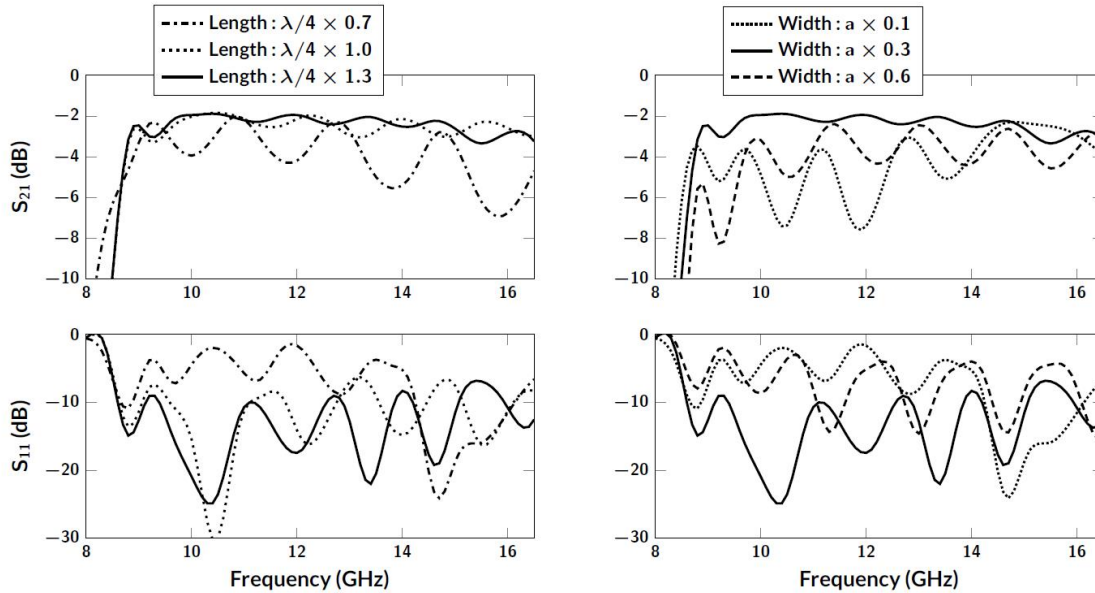


FIGURE 11 Evolution of the insertion losses S_{21} (up) and return losses S_{11} (down) simulated via COMSOL for an NSIW whose width is 6 mm and for a small subset of geometric parameters of the tapered transition. The simulations were conducted on a complete waveguide: a first transition, a 20 mm long NSIW waveguide and the final transition. Left: sweep on the taper length for a fixed taper width of $0.3 \times a = 1.8$ mm. The lengths are given as multiples of a quarter wavelength at the operational frequency of 12.5 GHz. Right: sweep on the taper width of a fixed taper length of $\lambda/4 \times 1.3 = 3.2$ mm. The taper widths are given as multiples of the waveguide width a . The two horizontal conductive planes of the NSIW are supposed to be perfect electrical conductors.

3.6.1 | Radiation losses

Because the vertical walls of the NSIW are not continuous, radiation leakage may flow between the vias. This leakage can significantly affect the global transmission quality if the vias geometry is not chosen carefully. Some studies have been conducted to describe, predict and reduce the radiation losses in classical SIW. They have resulted in simple geometric rules that have to be complied with to reduce the radiation losses^{12,43,44,45,46,47}. The geometric parameters of interest are the diameter d of the wires, the spacing s between them and the waveguide width a . They must be tuned in such a way to approximate the behavior of a continuous metallic wall: the spacing s of the vias has to remain small compared to their diameter d , while the diameter must be small compared to the waveguide width (or waveguide wavelength). To keep the radiation losses reasonably small,

TABLE 2 Values of the geometrical parameters for the optimized transition from 50 Ω coplanar line to a 6 mm wide NSIW, as shown in Figure 10.

Parameter	Dimension
CPWG ground width	500 μm
CPWG gap width	146 μm
CPWG track width	106 μm
CPWG length	500 μm
Taper length	3.1 mm
Taper width	1.8 mm
MS length	200 μm

the recommended values are given by(16)

$$s \leq 2d \quad ; \quad b \leq \frac{a}{5} \quad (16)$$

For a specific traveling mode, the leakage decreases with the increasing frequency and is maximal at the cut-off frequency of the mode. The radiation leakage factor α_R is independent of the substrate properties and independent of the height of the guide. In the end, the SIW shows comparable or lower losses as the other traditional planar structures like microstrip or coplanar lines especially at high frequencies¹³. If the substrate is thick enough, the losses are dominated by the dielectric behavior of the substrate. The condition (16) is not satisfied in the case of nanowired SIW. Indeed, typical values are $s = 100$ nm and $d = 40$ nm. However, it does not mean that we will observe a lot of leakage through the side walls. Indeed, the second rule, which recommends a vias diameter five times smaller than the guide width, is largely respected. But those geometric rules are empirical and were established for completely different SIW geometries where the vias diameter is of the same order of magnitude as the waveguide width. In the case of our NSIW, there are five orders of magnitude between these two dimensions. Hence, we can conclude that the two rules (16) do not apply to the NSIW case. Here, we have to keep in mind the discussion of the previous section: from the point of view of the EM wave, the walls are continuous (see Section 3.2). And, if their thickness is much higher than the skin depth, we will not get any radiation loss through the walls. It is worth to specify here that we will nonetheless observe radiation loss in the transition as the microstrip and coplanar topologies are unavoidably subject to such leakage radiation.

3.6.2 | Dielectric losses

Besides the radiation leakage which is almost non-existent in NSIW, other sources of losses exist: dielectric and conductive losses. The dielectric loss along a transmission line is given by expression (17) reported in¹⁷

$$\alpha_d = \frac{k^2 \tan \delta}{2\beta} \quad (17)$$

where $\tan \delta$ is the loss tangent of the dielectric, $k = \omega/c_0$ with c_0 light velocity is the wave vector, β the propagation constant. The dielectric loss increases linearly with the frequency once the cut-off frequency has been overpassed. For a 6 mm wide NSIW in nanoporous alumina membranes whose loss tangent is 1.5×10^{-2} , the dielectric is responsible for a loss of 0.68 dB/cm at 12.5 GHz. The only solution to decrease it would consist in changing the substrate itself.

3.6.3 | Conduction losses in NSIW

Obviously, conduction losses occur in the four metallic walls of the guide, namely the top and bottom horizontal metallic plates, and the two nanowired vertical walls. For a classical metallic rectangular waveguide, the attenuation due to conductor losses has the expression (18) reported in¹⁷

$$\alpha_c = \frac{1}{\beta k \eta} \left(R_{sh} \frac{2\pi^2}{a^3} + R_{sv} \frac{k^2}{b} \right) \quad (18)$$

where R_{sh} is the sheet resistance of the horizontal metallic planes of the waveguide while R_{sv} is for the two vertical metallic walls, and $\eta = \sqrt{\frac{\epsilon}{\mu}}$. Although the vertical walls are not fully metallic, their conductivity can be expressed as $p\sigma$ where p is the porosity of the template and σ is the conductivity of metal, so that we can write expression (19) reported in¹⁷

$$R_{sh} = \sqrt{\frac{\omega\mu}{2\sigma}} \quad R_{sv} = \sqrt{\frac{\omega\mu}{2p\sigma}} = \frac{R_{sh}}{\sqrt{p}} \quad (19)$$

The conductor losses can be expressed for convenience by expression (20)

$$\alpha_c = T_h + T_v = \frac{1}{\beta k \eta} \left(R_{sh} \frac{2\pi^2}{a^3} + R_{sh} \frac{k^2}{\sqrt{p}b} \right) \quad (20)$$

The evolutions with the frequency of T_h , associated with horizontal walls and T_v , associated with vertical walls, for a 6 mm wide NSIW are drawn in Figure 12a for three substrate thicknesses. We observe that T_v is 20 times lower than T_h : their values are respectively 0.0045 dB/cm and 0.092 dB/cm at 12.5 GHz with $b = 100 \mu\text{m}$. The conduction losses in the horizontal metallic plates are much higher than in the walls. In order to decrease T_h , a solution is to increase b . Indeed, given Equation (20), T_h is proportional to $1/b$. However, this solution is difficult to realize as it is conditioned by the availability of a suitable nanoporous substrate. The two terms T_h and T_v are also linked to the width of the guide a through the propagation constant: their evolutions with a are given in Figure 12b. To realize that figure, the terms have been evaluated at the operational frequency f_0 of the waveguide whose width is a . The conclusion for a is the same than for b : increasing the size of the NSIW decreases the losses. T_v stays smaller than T_h for all the concerned dimensions, excepted when a becomes smaller than $500 \mu\text{m}$.

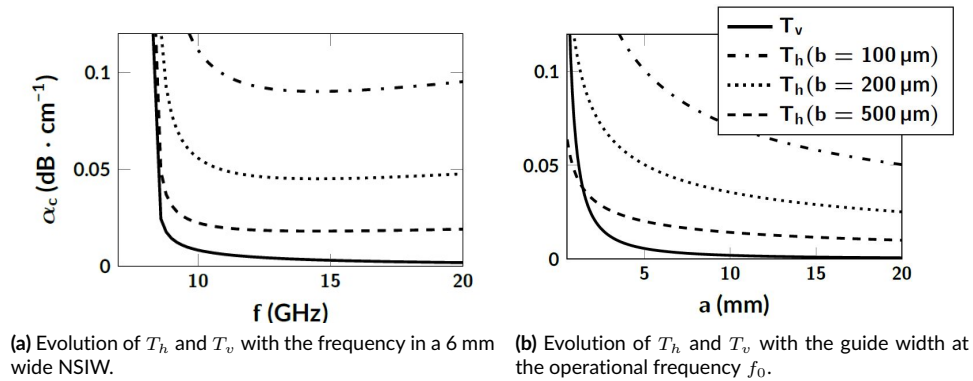


FIGURE 12 Evolution of the two terms of the conductive losses T_h and T_v in an NSIW for three various substrate heights. (a) Evolution with the frequency determined in a 6 mm wide NSIW. The first term of the conductive loss T_v is much lower than the second T_h . Given the definitions in Equation (20), increasing the substrate height b decreases T_h with $1/b$. (b) Evolution with the waveguide width a of T_h and T_v . The losses are calculated at the operational frequency f_0 given with Equation (9). T_h is also depending on b through β in (20). T_v becomes important only when $a \ll 5$ mm and is rapidly decaying when a becomes higher. T_h decreases with increasing a .

3.6.4 | Influence of roughness

The RF sheet resistance R_s describes the resistance at high frequencies of a thin metallic layer. For the study of NSIW, this concept is useful to characterize the loss due to surface currents in the Cu layers deposited onto both faces of the membrane. R_s is defined for a uniform layer and is largely depending on the conductivity of the material. It is obvious that if this conductivity is lower, the resistance will be higher and the conductive loss will be higher as well. This conductivity can be directly affected in different ways. For example, the microstructure, the density or the purity of the electroplated copper may not be optimal so that the properties of the layer are not as expected^{48,49}. Another reason for reduction in conductivity is the roughness that the Cu layer may have. Due to skin effect, the roughness affects directly the sheet resistance, and the effect is important at RF frequencies.

This is inconvenient because the steps of the experimental process, which include the use of the laser, make the nanoporous substrate highly rough. This is especially true in the case of the laser-patterning method based on the porosity destruction. It is doubtful that the laser, which crushes the top of the substrate to clog the pores, can leave a clean, flat, and smooth surface behind it. Therefore, when the copper layer is deposited onto the surface, it follows the shape of the surface. The roughness of the substrate is transferred to the copper layer. This transfer has not been studied in depth but three cases can be considered (see Figure 13).

Although intuitively unlikely, it is possible that the copper layer perfectly matches the profile of the membrane and properly reproduces it (see Figure 13a). In the same way, it is also possible that the copper layer completely cancels the roughness so that the top of the copper layer is smooth (see Figure 13b). These two situations are extreme and unlikely cases. A more credible situation is that the deposited copper partially smooths the surface (see Figure 13c). The layer does not perfectly follow the shape of the surface because its thickness is similar to the RMS roughness of the surface.

In any case, the roughness of the copper layer cannot be higher than that of the template. The roughness in question here is that of the underside of the $5 \mu\text{m}$ thick copper layer, i.e. between copper and alumina. Measuring it is a complicated matter and will not be discussed here. But, if we

measure the roughness of the AAO, we can deduce an approximation of the one of copper. In the following, it is assumed that the roughness of the copper layer is within the same range of values as the template itself.

The roughness of the template after the etching was characterized using profilometers. RMS roughnesses between 1 μm and 5 μm were measured. This roughness is not constant and varies from one sample to another given the variations in the laser process. Given these considerations, it seems appropriate to study how transmission within the waveguide is affected by the roughness of the copper layer. This is the purpose of the following section.

To take it into account, the definition of R_s (19) can be modified by a factor depending on the roughness. Two approaches are described below.

Hammerstad model

The simplest way to characterize the transmission through rough structures is the Hammerstad's model introduced by Hammerstad and Bekkadal in 1975^{50,51}. It proposes a modification (21) of the definition of the sheet resistance R_s (19) by a factor depending on Δ , the root mean square (RMS) roughness of the metallic layer:

$$R_s(\Delta) = R_s \left(1 + \frac{2}{\pi} \arctan \left(1.4 \left(\frac{\Delta}{\delta} \right)^2 \right) \right) \quad (21)$$

where δ is the skin depth. According to that model, when the RMS roughness reaches the skin depth, the conduction losses are increased by 60 %. If the RMS roughness is much larger than the skin depth, losses are at most doubled. Moreover, when the frequency becomes important, δ decreases subsequently and R_s also converges towards 2. This convergence of the sheet resistance for high roughness and/or high frequencies is one of the disadvantages of the Hammerstad model.

Gradient model

Another recently introduced model, the Gradient Model⁴⁰, proposes a definition of three parameters of a rough surface: its effective conductivity σ_{eff} , its effective permeability μ_{eff} and its surface impedance Z_s . The surface of metal is described by a cumulated density function of the matter at its border. The DC conductivity becomes depending on the depth into the metal, decreasing from its bulk value to zero at a rate similar to the evolution of the density of matter. This location-dependent conductivity $\sigma(x)$ is then used to solve Maxwell's equation to obtain the evolution of the magnetic field near the surface. The effective conductivity σ_{eff} is obtained by equalizing the loss power density of the rough surface with the location-dependent conductivity $\sigma(x)$ and the loss power density of a perfectly smooth surface with the effective conductivity σ_{eff} . The surface impedance Z_s (which real part corresponds to the surface resistance R_s) is determined by dividing the electric and magnetic fields obtained from Maxwell's equation solved with $\sigma(x)$ and time-harmonic fields. In the end, all the proposed parameters depend only on the RMS surface roughness Δ and its bulk conductivity σ .

It may be recalled that the real part of the surface impedance $\text{Re}(Z_s)$ is equal to its sheet resistance R_s . The sheet resistance computed with the classical formula (see Equation (18)) using the effective conductivity σ_{eff} obtained from the Gradient Model matches perfectly with the real part of the proposed surface impedance Z_s while these two quantities are calculated with different methods.

The evolutions with the frequency of the effective conductivity σ_{eff} and the sheet resistance R_s are given in Figure 14 for a copper surface whose DC conductivity is 56 10^6 S/m. The influence of the roughnesses on both parameters is important. According to the Gradient Model, the conductivity of the copper surface at 10 GHz is reduced to 22.48 10^6 S/m for $\Delta = 500$ nm, 9.82 10^6 S/m for $\Delta = 1000$ nm, and to 0.87MS 10^6 S/m for $\Delta = 5000$ nm. The sheet resistance increases with increasing Δ . At 10 GHz, R_s is multiplied by 2 if $\Delta = 1000$ nm and by nearly 10 if $\Delta = 5000$ nm.

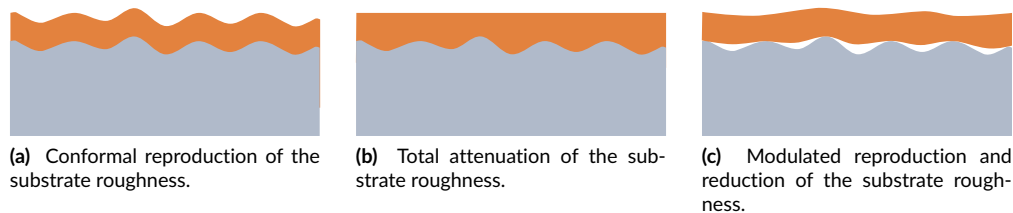


FIGURE 13 Three scenarios of the deposition of a copper layer onto a rough substrate. In orange, the copper layer. In grey, the AAO substrate. A copper seed layer is first deposited onto the alumina. This is then thickened by electrodeposition. The roughness of the substrate comes from the laser treatment that clogs the nanopores, but also strongly affects the surface.

Once the sheet resistance of the rough surface copper has been determined, it can be inserted into Equations (19) and (20) to describe the losses into the NSIW. However, this must be done carefully because, as already mentioned, the four walls of an NSIW are not identical. The modified sheet resistance R_S^{GMs} can only be inserted into the second term T_h standing for the loss in the two horizontal copper plates of the NSIW. The term T_v is not modified by the roughness. At least two reasons explain this. First, to obtain its results, the Gradient Model assumed a translational invariance in the two basis directions of the studied surface. But the walls are made with nanowires which are elongated structures, and a translational symmetry can only be assumed in the vertical y direction. Secondly, given the laser patterning method, the walls are precisely defined. Their roughness is much lower than the roughness of the horizontal plates. In any case, this distinction is not very relevant in this present situation. Indeed, we could also increase the resistance of the T_v term, it would not change the result because it is much lower than T_h .

It has been shown that this model accurately predicts the propagation characteristics (attenuation and phase delay) along various transmission lines and for high roughnesses. As this model handles directly the conductivity of the metallic layer, it is independent of the structure of the transmission line. The effective conductivity is used in place of the bulk one and is inserted in the definition of sheet resistance (18). Hence, the Gradient Model can be used to characterize the conductive loss in the NSIW.

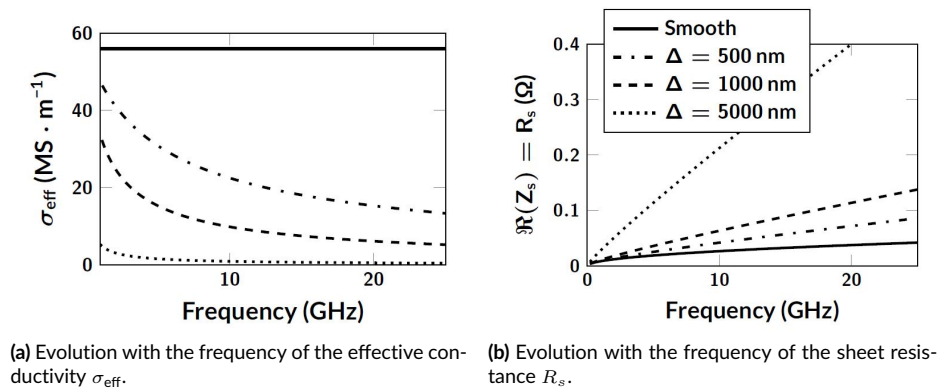


FIGURE 14 Evolution with the frequency of the effective conductivity σ_{eff} (a) and the sheet resistance R_s (b) given by the Gradient Model for three RMS roughnesses Δ . The values of the DC conductivity of a smooth copper surface and its associated sheet resistance are given for comparison. The sheet resistance computed with the classical formula (19) using the effective conductivity σ_{eff} is identical to the real part of the surface impedance given by the Gradient Model. According to that model, the conductivity of a rough surface decreases drastically when Δ increases. Subsequently, its sheet resistance (or surface impedance) increases with Δ .

Comparison

The conductive loss as a function of the frequency is depicted in Figure 15. The perfectly smooth case, the Hammerstad's model and the Gradient Model are compared. The shown losses are the sum of the two terms T_v and T_h defined in Equation (20). Hence, the lowest curve α_c is the sum of the blue and green curves of Figure 12a. The modified definition of Hammerstad (21) of the sheet resistance gives rise to a modified conductive loss depending on the roughness denoted α_c^H . The Gradient Model has also been implemented to deduce the sheet resistance so as to finally give a corrected definition of the conductive loss designated by α_c^{GM} . The classical definition (20) of conductive loss α_c , without any modification due to roughness is also drawn as a reference. The curves are plotted for a 6 mm wide NSIW embedded in a 100 μm thick AAO membrane. Two different roughnesses have been considered. The dashed line stands for $\Delta = 1 \mu\text{m}$ while the solid line is for $\Delta = 5 \mu\text{m}$. As expected, the difference between the two models increases when the roughness reaches high values while α_c is unchanged. When the RMS roughness is about 5 μm , α_c^{GM} is at least multiplied by six. As for the uncorrected loss α_c , α_c^{GM} decreases rapidly after the cut-off frequency. However, a few gigahertz further on, it reaches a minimum and begins to increase. An important observation is that, according to the Gradient Model, the minimum of the conductive loss is reached around 12.5 GHz, which is the operational frequency of the considered nanowired waveguide. This observation was confirmed for a range of NSIW widths going from 1 mm up to 20 mm and for a wide range of roughnesses.

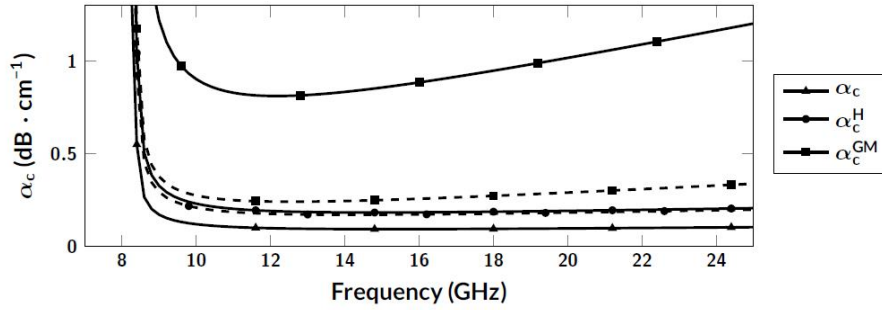


FIGURE 15 Evolution with the frequency of the conductive loss for various implementation of the impact of the roughness: α_c^{GM} , α_c^H and α_c stand for, respectively, the Gradient Model³⁹, Hammerstad's model given in (21) and the unmodified conductive loss given by (20). The curves are drawn for a 6 mm wide NSIW and two different RMS roughnesses: 1 μm (dashed line) and 5 μm (solid line). The loss drawn here is the sum of the two terms T_v and T_h defined in (20). The Gradient Model predicts a significant rise of the conductive loss as the RMS roughness increases and this rise is higher at higher frequencies. The Hammerstad's model predicts a convergence of the loss at high roughness and high frequency.

3.7 | Losses in transitions

The loss mechanisms discussed in the previous section only concern the NSIW waveguides guide themselves, while these devices are always connected with two transitions as discussed before. Below, we will examine the losses in these transitions. The problem, seen from an analytical point of view, is not easy to deal with. The transitions are composed of different sections of different line topologies, along which various modes can propagate. It is therefore complicated, if not impossible, to deduce analytical formulas similar to Equation (20). Indeed, this formula is only valid for TE₁₀ mode in a rectangular cavity. Though, in transitions, various modes are propagating along with various topologies. To circumvent this issue, it is convenient to use FEM simulations to deduce the losses in the transitions. Indeed, this kind of simulation does not require to assume that the wave is a sum of particular modes.

As seen in the previous paragraphs, the conductivity of the metallic layers can be lowered because of the roughness. Moreover, the microstructure or the density of the metal may also affect the conductivity of the electroplated copper. Finally, all of this can be modeled by modifying directly the conductivity of the copper layer. In Figure 16, the transmission evaluated through NSIW structure, noted S_{21} , is given for various roughnesses, implemented in the FEM model through the conductivity of the horizontal metallic layers. Those results were produced by full-wave FEM simulations using COMSOL. The horizontal metallic layers are 5 μm thick. In continuous line, S_{21} is simulated for a 20 mm long NSIW cavity only while the dashed line gives S_{21} for an NSIW with its transitions. In the case of the NSIW without its transitions, the propagating modes are excited with the appropriate boundary conditions. We observe that the transmission is lowered when the roughness is increasing, i.e. when the conductivity of the layer is decreasing. The loss of power in the transitions is increasing faster than the conductivity decreases. For PEC layers, there are only 0.71 dB lost at 12.5 GHz because of the transitions, while they are 1 dB at the same frequency when $\Delta = 500$ nm, 1.26 dB when $\Delta = 1000$ nm and 3.31 dB when $\Delta = 5000$ nm. Hence, if the conductivity of the metallic layer becomes very poor, the loss in the transition will be very high and will increase rapidly with the frequency.

Another important observation from Figure 16 is related to the cut-off frequency. The dashed lines (corresponding to NSIW devices with transitions) start to decrease at a frequency which is difficult to identify precisely: the cut-off effect is less clear when transitions are present. In addition, the increasing roughness accentuates this difficulty. Hence, while the cut-off of the PEC waveguide without the transitions appears near 8.3 GHz which is the theoretical value, it becomes close to 10 GHz for the waveguide with transition and high RMS roughness ($\Delta = 5000$ nm).

From the S parameters measured along any waveguide of length L , the losses per unit length α can be deduced through the formula (22)

$$\alpha = -\frac{1}{L} \left(\frac{|S_{21}|^2}{1 - |S_{11}|^2} \right) \quad (22)$$

where α takes into account all kind of losses: radiation, dielectric and conduction losses. This formula allows creating Figure 17 where α has been deduced from the data of Figure 16 in the case of the NSIW without its transitions. In addition, the theoretical dielectric losses have been plotted. As seen previously, there are no radiation leakages along an NSIW. Then, when the conduction loss is very low (i.e. when the conductivity is very high), only the dielectric loss is important. As expected, the dielectric loss is equivalent to the total loss that is induced along the line with PEC conductive layers. These losses are 0.68 dB/cm: even if the copper layers are perfect, measuring losses lower than this value is impossible. The total loss increases rapidly if the conductivity of the metallic layer is not at its optimal value. The conductivity of these layers is decreased by their roughness. The losses increase until 3 dB/cm for very high roughness. To keep the transmission as good as possible, it is therefore important to pay attention to keep the Cu layers as smooth and as conductive as possible.

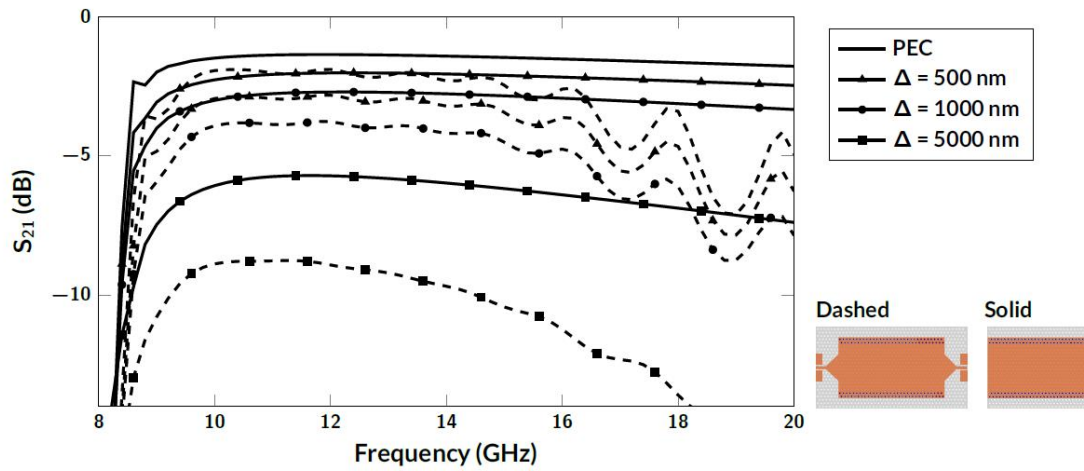


FIGURE 16 Evolution with the frequency of the transmission parameter S_{21} simulated through a 6 mm wide NSIW without (continuous line) and with (dashed line) its connecting transitions. The transmission through both structures were simulated for three values of Δ , the RMS roughness of the 5 μm thick horizontal copper layers situated on both sides of the membrane. The implementation of the roughness is made by varying the effective conductivity of the copper layer, according to the Gradient Model (see in the text). The values of the three frequency-dependent conductivities of the copper layer are given in Figure 15. According to that model, the conductivity of a rough surface decays with the frequency. The transmission through an NSIW with perfectly smooth and perfect electrical conductor (PEC) copper layer is given for comparison. The difference between the transmissions through an NSIW with or without its transitions increases with Δ and with the frequency. Hence, optimizing the transitions is more and more important when the roughness increases.

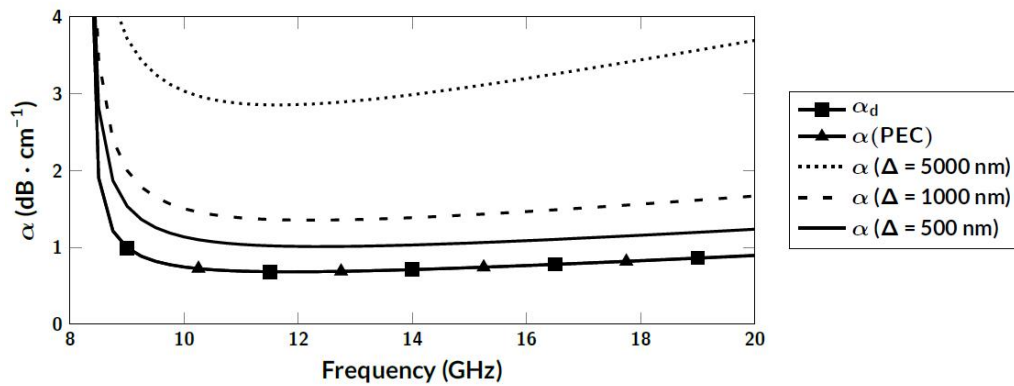


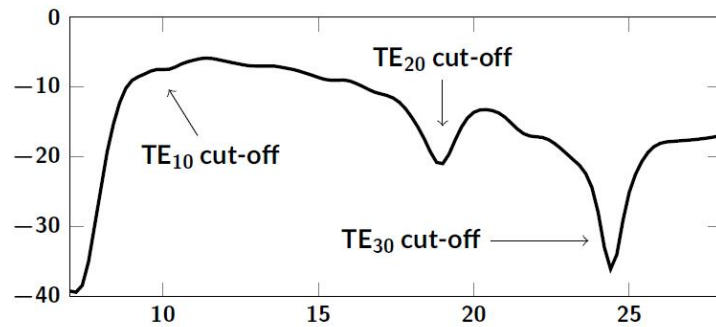
FIGURE 17 Evolution with the frequency of losses per unit length in a 6 mm wide NSIW. The theoretical dielectric loss α_d is given as well as the total loss for PEC copper layers and three roughnesses, corresponding to three conductivities. The total loss is evaluated with FEM simulation. Those data are taken from Figure 16 (without the transitions) and α is obtained with Equation (20). For PEC metallic layers, the total loss (evaluated by FEM simulations) is equivalent to the dielectric loss given by Equation (17). Though, this total loss increases drastically for decreasing conductivity, i.e. increasing roughness.

4 | EXAMPLES OF DESIGNS

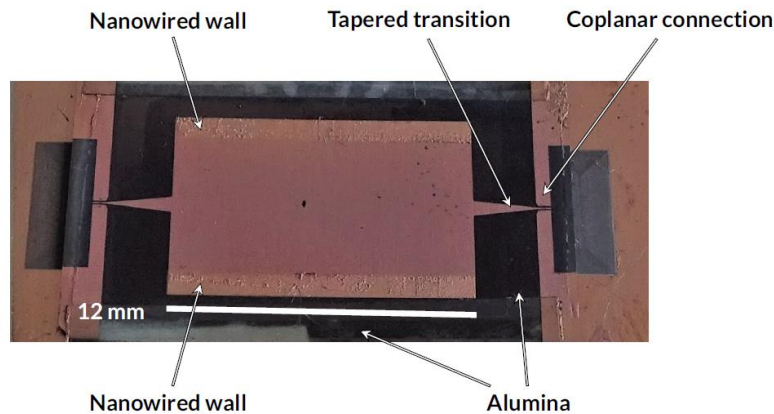
The parametric study presented in the previous section serves as a basis for our design and fabrication of numerous NSIW devices, including transmission lines, filters and non-reciprocal isolators. Two examples are illustrated in the following: an NSIW line and an EBG (Electromagnetic Band Gap) filter.

4.1 | NSIW line

The geometry of the NSIW line is illustrated in Figure 1. Its realization including two taper microstrip lines for its measurement, and the measurement itself, is shown in Figure 18 and fully described in³⁹. Three cut-off frequencies can be observed. The first one located at 8.4 GHz can be successfully compared with the prediction of cut-off frequencies $f_{c10} = 8.33$ GHz using Equation (8), as well as the third one at 24.5 GHz. They are obtained considering in Equation (10) the porosity p of the membrane equal to 9.08 %, which fixes the value of dielectric constant: $\epsilon = 9$. Also, the center frequency predicted by Equation (9) is very close to the experimental observation, i.e $f_0 = 12.5$ GHz. This illustrates that the nanowired walls discussed in Section 3.2 act as efficient shielding generating the expected behavior of the metallic RW. Indeed the width of the realised walls is 1 mm, well above the 10 microns expected in Section 3.2.



(a) Measured transmission through a 12 mm long substrate integrated nanowired waveguide. Two walls made of nanowires define a 6 mm wide cavity guiding the signal and inducing a cut-off effect at 9.5 GHz, as predicted by the theory.



(b) Photograph of a fabricated nanowired substrate integrated waveguide embedded in an alumina template. The cavity is 12 mm long and is embedded between two triangular tapered microstrip transitions, each connected to rectangular contact pads for the CPWG measuring probes. The nanowire arrays have been grown in the template using the laser-patterning method based on the clogging of the pores by porosity destruction. The copper layer on top of the template is also etched using the laser.

FIGURE 18

Meanwhile, the insertion loss observed is - 8 dB. Although being important, they are closely related to the rugosity effect observed in Figure 16. A similar level is observed for a simulated RMS rugosity equal to 5000 nm. Such a rugosity can be easily explained by the porosity of the membrane. As explained before, during the electrodeposition of metal on top and bottom faces of the membrane in order to fabricate the device of Figure 1, some metal enters the pores, causing the formation of metallic layers that have a non-uniform thickness.

4.2 | NSIW EBG filter

The EBG filtering effect is generated by an arrangement of transmission lines sections having periodical alternations of dielectric constants. In the case of NSIW devices, the alternations are created by exploiting the effect described in¹⁹. Compared with that of porous alumina, the dielectric constant of the alumina template can be increased drastically when the porous membrane is filled by conductive nanowires over a portion h_f of the membrane height $h_{AAO} = b$, according to Figure 19a. In our previous works^{54,55,56} we discussed the influence of partially filled pores on the design and performances of microwave devices based on nanowires. Here we illustrate that the partially filled pores can be used as an advantage for the design of microwaves devices.

The principle illustrated in Figure 19b is based on Equation (23). It provides the complex dielectric constant of the AAO template having a porosity $p = 11\%$ and partially filled with nickel nanowires.

$$\frac{1}{\varepsilon_{rNW}} = \frac{h}{\varepsilon_{rw}} + \frac{1-h}{\varepsilon_{rAAO}} \quad (23)$$

where $h = h_f/h_{AAO}$ is the ratio of wire height h_f to AAO thickness, ε_{rAAO} is the dielectric constant of porous alumina template given by Equation (10) and ε_{rw} is the dielectric constant of the AAO filled with nanowires, obtained by replacing in Equation (10) ε_{rair} by the dielectric constant of nanowires, namely $\varepsilon_{rw} = 1 - j\sigma/\omega/\varepsilon_0$, with $\omega = 2\pi f$ and ε_0 is the permittivity of vacuum.

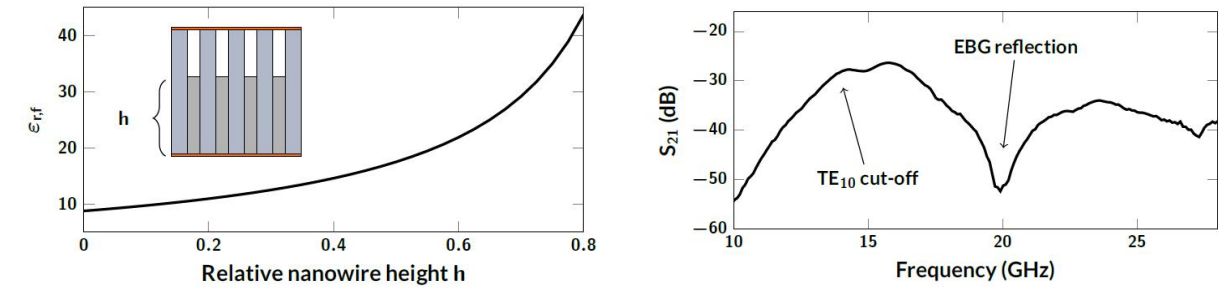
Figure 19a shows the corresponding dielectric constant noted ε_{rNW} as a function of the filling factor h . For $h = 0.75$, the dielectric constant of the filled area, noted ε_{rNW} is equal to 34, while those of the porous anodic alumina, noted ε_{rAAO} is equal to 8.8, as provided from the value at zero h in Figure 19a. The NSIW filter is built by posting 3 rectangular areas of length L_{NW} , that are filled with Ni nanowires over 75% of AAO thickness h_{AAO} and are separated by a distance L_{AAO} , corresponding to porous AAO areas (Figure 20). The cascade of dielectric constants over the length of the EBG device is given by expression (24):

$$\varepsilon_{rNW} = 34; \quad \varepsilon_{rAAO} = 8.8; \quad \varepsilon_{rNW} = 34; \quad \varepsilon_{rAAO} = 8.8; \quad \varepsilon_{rNW} = 34 \quad (24)$$

denoting a high contrast between dielectric constants. The EBG effect is induced due to this contrast at frequency $f_0 = 20$ GHz if the length of each section L_{AAO} or L_{NW} is equal to a quarter wavelength at f_0 , i.e expressions (25):

$$L_{AAO} = \frac{\lambda_a}{4} = \frac{c_0}{f_0 \sqrt{\varepsilon_{rAAO}}} = 5.1 \text{ mm} ; \quad L_{NW} = \frac{\lambda_{NW}}{4} = \frac{c_0}{f_0 \sqrt{\varepsilon_{rNW}}} = 2.6 \text{ mm} \quad (25)$$

where c_0 is the light velocity in air.



(a) Dielectric constant of AAO template filled with nanowires having a relative height $h = h_f/h_{AAO}$.

(b) Measured transmission through an NSIW loaded with three EBG strips. The two walls of nanowires define a 3 mm wide cavity guiding the signal and inducing a cut-off effect. The length of the strips and their spacing have been determined to create a reflection at 20 GHz.

FIGURE 19

Figure 19b demonstrates the validity of the above design for an NSIW having a width a equal to 3 mm. This value moves the operational bandwidth in the 16-32 GHz range. A deep in transmission S_{21} is observed exactly at 20 GHz, as expected from the design, denoting the blocking of the signal, which is characteristic of a bandgap effect.

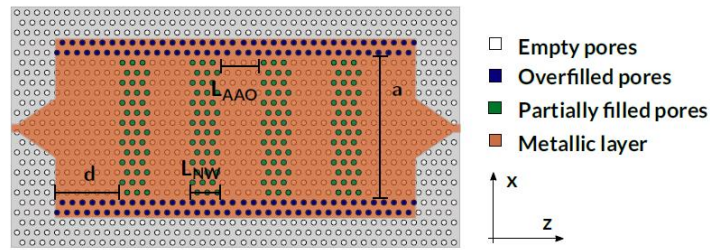


FIGURE 20 Schematic top-view of a nanowired substrate integrated filter based on electromagnetic band-gap effect. In blue, the overfilled nanowire arrays short cut the top and bottom faces of the waveguide. In green, the metallic nanowires placed along the guide induce successive reflections. The distance L_{AAO} between the transverse strips and the length L_{NW} of those strips are tuned to induce reflections and a filtering effect at a precise frequency. The first strip is placed at a distance d of the beginning of the waveguide, whose width is a .

5 | CONCLUSIONS

The paper presented a parametric study of the factors influencing the behavior and performances of NSIW devices. Various physical and geometrical parameters were investigated, using analytical models combined with FEM simulations. This allowed establishing guidelines for NSIW devices. The approach was illustrated by the design of two NSIW devices: an NSIW line, and an EBG NSIW filter.

The first conclusion of our work is that transitions are sources of losses. They considerably affect the propagation of signals. It is theoretically possible to remove their influence by de-embedding methods. These methods are based on the measurement of different identical lines but of different lengths. But this is complicated due to reproducibility problems. However, it should be noted that the ultimate goal of our work is the design of a complete platform of integrated circuits in NSIW topology, combining filters, antennas, lines, isolators or circulators, etc. In this perspective, transitions between different topologies should be limited or even absent. Artifacts associated with these transitions will then also disappear.

Secondly, the roughness of the alumina membrane is pointed out. This is directly created by the experimental process. It is indeed difficult to imagine that the laser would leave a smooth membrane behind it. Switching to conventional lithography techniques would be a good alternative. This makes the process longer, more complex, and more expensive. However, it seems to be the right way to reach performances that rival the state-of-the-art. Some practical problems will have to be solved beforehand, such as the compatibility between the alumina membranes and the lithography setup built for silicon wafers. But this is not a blocking issue on the principle.

Finally, an architecture of hollow waveguide would allow reducing insertion losses; we have thought about such a solution but in our case nanowires are necessary inside the waveguide to achieve microwave functions. Alumina should be etched in areas where nanowires are not necessary, which is not an easy task. Besides, a top metal cover must be reconstructed after etching alumina, which is not evident.

ACKNOWLEDGMENTS

This work was supported by the Research Science Foundation of Belgium (FRS-FNRS). VVK acknowledges the FRS-FNRS for financial support (FRIA grant). IH is Research Director at FRS-FNRS. VVK is grateful to G. Gold and K. Helmreich for providing the conductivity data using the Gradient Model, for different roughnesses.

Author contributions

Design, fabrication and experimental characterization, writing: V. Van Kerchoven. Writing and supervision: L. Piraux and I. Huynen.

Financial disclosure

None reported.

Conflict of interest

The authors declare no potential conflict of interests.

Data Availability Statement

The data that support the findings of this study are available from the corresponding author upon reasonable request.

References

1. L. Qiao, X. Han, B. Gao, J. Wang, F. Wen, and F. Li, Microwave absorption properties of the hierarchically branched Ni nanowire composites. *Journal of Applied Physics* **2009**, *105*, 053911.
2. W. Chen, M. Han, and L. Deng, High frequency microwave absorbing properties of cobalt nanowires with transverse magnetocrystalline anisotropy. *Physica B: Condensed Matter* **2010**, *405*, 1484-1488.
3. G. Hamoir, L. Piraux, and I. Huynen, Q-factor improvement of integrated inductors using high aspect ratio ferromagnetic nanowires. *Microw. Opt. Technol. Lett.*, **2012**, *54*, 1484-1488.
4. B. Kuanr, V. Veerakumar, R. Marson, S. Mishra, A. Kuanr, R. Camley and Z. Celinski, Nickel Nano-Wires Filled Alumina Templates for Microwave Electronics. *IEEE Trans. Magn. Lett.*, **2009**, *45*, 4052-4055.
5. A. Saib, D. Vanhoenacker-Janvier, I. Huynen, A. Encinas, L. Piraux, E. Ferain, and R. Legras, Magnetic photonic band-gap material at microwave frequencies based on ferromagnetic nanowires. *Appl. Phys. Lett.* **2003**, *83*, 2378.
6. A. Saib, M. Darques, L. Piraux, D. Vanhoenacker-Janvier, and I. Huynen, An unbiased integrated microstrip circulator based on magnetic nanowired substrate. *IEEE Trans. Microwave Theory Tech.* **2003**, *83*, 2378.
7. L. Carignan, C. Caloz, and D. Menard, Dual-band integrated self-biased edge-mode isolator based on the double ferromagnetic resonance of a bistable nanowire substrate. *Microwave Theory and Techniques, IEEE Symposium Digest* **2010**, 1336-1339.
8. G. Hamoir, J. De La Torre Medina, L. Piraux, and I. Huynen, Self-Biased Nonreciprocal Microstrip Phase Shifter on Magnetic Nanowired Substrate Suitable for Gyrator Applications. *IEEE Trans. Microwave Theory Techn.* **2012**, *60*, 152-157.
9. A. Serrano, A.-L. Franc, D. Assis, F. Podevin, G. Rehder, N. Corrao, and P. Ferrari, Slow-wave microstrip line on nanowire-based alumina membrane. *Microwave Symposium (IMS), 2014 IEEE MTT-S International*. **2014**, 1-4.
10. J. Spiegel, J. De La Torre, M. Darques, L. Piraux, and I. Huynen, Permittivity Model for Ferromagnetic Nanowired Substrates. *IEEE Microwave and Wireless Components Letters* **2007**, *60*, 492-494.
11. R. Ramirez-Villegas, I. Huynen, L. Piraux, A. Encinas, and J. D. L. T. Medina, Self-Biased Nonreciprocal Microstrip Phase Shifter on Magnetic Nanowired Substrate Suitable for Gyrator Applications. *IEEE Trans. Microwave Theory Techn.* **2016**, *65*, 72-77.
12. K. Wu, D. Deslandes, and Y. Cassivi, The substrate integrated circuits - a new concept for high-frequency electronics and optoelectronics. *Int. Conf. Telecommunications in Modern Satellite, Cable and Broadcasting Service* **2003**, *60*, III-X.
13. M. Bozzi, A. Georgiadis, and K. Wu, Review of substrate-integrated waveguide circuits and antennas. *IET Microwaves, Antennas and Propagation* **2011**, *5*, 909.
14. R. Moro, M. Bozzi, A. Collado, A. Georgiadis, and S. Via, Plastic-based Substrate Integrated Waveguide (SIW) components and antennas. *Proc. European Microwave integrated circuits Conference* **2012**, *65*, 627-630.
15. V. Van Kerckhoven, L. Piraux, and I. Huynen, Substrate integrated waveguide isolator based on ferromagnetic nanowires in porous alumina template. *App. Phys. Lett.* **2014**, *105*, 183107.
16. V. Van Kerckhoven, L. Piraux, and I. Huynen, A laser-assisted process to produce patterned growth of vertically aligned nanowire arrays for monolithic microwave integrated devices. *Nanotechnology* **2016**, *65*, 72-77.
17. D. Pozar, *Microwave Engineering 4th edition* **2012**.
18. G. Hamoir. Microwave Devices Based on Unbiased Tunable Ferromagnetic Nanowire Arrays. *PhD Thesis*. Université catholique de Louvain **2014**.

19. O. Lasers. J-1064/355 System - Operation Manual. Tech. Rep. **2010**.
20. A. Emplit, E. Tooten, V. Xhurdebise, I. Huynen, Multifunctional material structures based on laser etched carbon nanotubes arrays. Micromachines, **2014**, 5, 756-765.
21. H. Eul and B. Schiek, Reducing the Number of Calibration Standards for Network Analyzer Calibration. IEEE Transactions on Instrumentation and Measurement **1991**, 40, 732-735.
22. V. Van Kerckhoven, L. Piraux, I. Huynen, A novel laser-assisted fabrication process for nanowired substrate integrated devices. Proceedings of the EuMic Conference **2018**, 170-173.
23. S. Raman, F. Rucky, and G. Rebeiz, A High-Performance W-Band Uniplanar Subharmonic Mixer. IEEE Trans. Microwave Theory Techn. **1997**, 45, 955-959.
24. J. Kim, Y. Qian, G. Feng, P. Ma, J. Judy, M. Frank Chang and Tatsuo Itoh, A Novel Low-Loss Low-Crosstalk Interconnect for Broad-Band Mixed-Signal Silicon MMIC's. IEEE Trans. Microwave Theory Techn. **1999**, 47, 1830-1834.
25. D. Dancila, X. Rottenberg, H. A. C. Tilmans, W. De Raedt and I. Huynen, 57-64 GHz Seven-Pole Bandpass Filter Substrate Integrated Waveguide (SIW) in LTCC. Proceedings of the 2011 IEEE MTT-S International Microwave Workshop on Millimeter Wave Integration Technologies **2011**, 200-203.
26. H. M. Hizan, Z. Ambak, A. Ibrahim, M.Z.M. Yusoff, T. Kanesan, Effect of Insertion Losses on Millimeter-Wave SIW Filters Using LTCC Technology. Proceedings of the 2015 IEEE International RF and Microwave Conference (RFM 2015) **2015**, 64-68.
27. M. Bertrand, G. P. Rehder, A. L. C. Serrano, L. G. Gomes, J. M. Pinheiro, R. C. A. Alvarenga, N. Kabbani, D. Kaddour, V. Puyal, P. Ferrari, Integrated Waveguides in Nanoporous Alumina Membrane for Millimeter-Wave Interposer. IEEE Microwave and Wireless Components Letters **2019**, 29, 83-87.
28. M. Pasian, M. Bozzi, L. Perregrini, Crosstalk in Substrate Integrated Waveguides. IEEE Trans. Electromagnetic Compatibility. **2015**, 57, 80-86.
29. Q.H Lai, C. Fumeaux, W. Hong, Mutual coupling between parallel half-mode substrate integrated waveguides. 2012 International Conference on Microwave and Millimeter Wave Technology (ICMMT), **2012**, 5, 4 p.
30. J. J. Simpson, A. Taflove, J.A. Mix, H. Heck, Substrate integrated waveguides optimized for ultrahigh-speed digital interconnects. IEEE Trans. Microwave Theory Tech. **2006**, 54, 1983-1990.
31. T. Djerafi, A. Doghri and K. Wu, Handbook of Antenna Technologies. Springer Science+Business Media Singapore **2005**, Chapter 5.
32. P. Debnath, S. Chatterjee, Substrate integrated waveguide antennas and arrays. 2017 1st International Conference on Electronics, Materials Engineering and Nano-Technology (IEMENTech) (ICMMT), Kolkata, India **2017**, 6 p.
33. A. Kumar and S. Raghavan, A Review: Substrate Integrated Waveguide Antennas and Arrays. Journal of Telecommunication, Electronic and Computer Engineering. **2016**, 8, 95-104.
34. N. Ashraf, O. Haraz, M. A. Ashraf and S. Alshebeili, 28/38-GHz dual-band millimeter wave SIW array antenna with EBG structures for 5G applications. International Conference on Information and Communication Technology Research (ICTRC) **2015**, 4 p.
35. E. Ghahramani, R. A. Sadeghzadeh, B. Boroomandisorkhabi and M. Karami, Reducing mutual coupling of SIW slot array antenna using uniplanar compact EBG (UC-EBG) structure. The 8th European Conference on Antennas and Propagation (EuCAP 2014) **2018**, 2002-2004.
36. D. Lopez, A. Coves, E. Bronchalo, G. Torregrosa, M. Bozzi, Practical Design of a Band-Pass Filter Using EBG SIW technology. The 48th Microwave European Conference **2018**, 77-80.
37. D. Li, C. Tong, J. Bao, P. Peng, and D. Yu, Compact EBG structure for alleviating mutual coupling between patch antenna array elements. Progress In Electromagnetics Research Letters, **2013**, 36 191-200.
38. Meng-Xia Yu and Zhen-Zhen Shi, A novel millimetre wave EBG-SIW wideband delay line,. International Journal of Electronics **2013**, 100 762-769.

39. V. Van Kerckhoven, L. Piraux, I. Huynen, Fabrication of Microwave Devices Based on Magnetic Nanowires Using a Laser-Assisted Process. *Micromachines* **2019**, *10* 16 p.
40. G. Gold and K. Helmreich. A Physical Surface Roughness Model and Its Applications. *IEEE Trans. Microwave Theory Tech.* **2017** *65* 3720-3732.
41. M. Bozzi, A. Georgiadis, and K. Wu, Review of Substrate-Integrated Waveguide Circuits and Antennas. *IET Microwaves, Antennas and Propagation* **2011** *5* 909.
42. Y. Cassivi, L. Perregrini, P. Arcioni, M. Bressan, K. Wu, and G. Conciauro, Dispersion Characteristics of Substrate Integrated Rectangular Waveguide. *IEEE Microwave and Wireless Components Letters* **2002** *12* 333-335.
43. F. Xu and K. Wu, Guided-Wave and Leakage Characteristics of Substrate Integrated Waveguide. *IEEE Trans. Microwave Theory Tech.* **2005** *53* 66-73.
44. M. Bozzi, L. Perregrini, and K. Wu, Modeling of Conductor, Dielectric, and Radiation Losses in Substrate Integrated Waveguide by the Boundary Integral-Resonant Mode Expansion Method. *IEEE Trans. Microwave Theory Tech.* **2008** *56* 3153-3161.
45. K. Lomakin, G. Gold, and K. Helmreich, Analytical Waveguide Model Precisely Predicting Loss and Delay Including Surface Roughness. *IEEE Trans. Microwave Theory Tech.* **66** 2018 pp. 2649-2662.
46. W. Che, D. Wang, K. Deng, and Y. L. Chow, Leakage and Ohmic Losses Investigation in Substrate-Integrated Waveguide. *Radio Science* **45** 2017.
47. M. Bozzi, M. Pasian, L. Perregrini, and K. Wu, On the Losses in Substrate-Integrated Waveguides and Cavities. *International Journal of Microwave and Wireless Technologies* **1** 2009 395.
48. L. Lu, Y. Shen, X. Chen, L. Qian, and K. Lu, Ultrahigh Strength and High Electrical Conductivity in Copper. *Science* **304** 2004 422-426.
49. L. Lu, R. Schwaiger, Z. Shan, M. Dao, K. Lu, and S. Suresh, Nano-Sized Twins Induce High Rate Sensitivity of Flow Stress in Pure Copper. *Acta Materialia* **53** 2005 2169-2179.
50. E. O. Hammerstad and F. Bekkadal. Microstrip Handbook. *Norwegian Institute of Technology* 1975.
51. E. Hammerstad and O. Jensen, Accurate Models for Microstrip Computer-Aided Design. *MTT-S International Microwave Symposium Digest*. **80**. 1980 407-409.
52. A. Coves et al. A novel band-pass filter based on a periodically drilled SIW structure, *Radio Sci.*, vol. 51, pp. 328-336, Apr. 2016.
53. L. Jin, R. M. A. Lee, and I. Robertson. Analysis and design of a novel low-loss hollow substrate integrated waveguide, *IEEE Trans. Microw. Theory Techn.*, vol. 62, no. 8, pp. 1616-1624, Aug. 2014.
54. G. Hamoir, L. Piraux, I. Huynen. Control of Microwave Circulation using Unbiased Ferromagnetic Nanowires Arrays, *IEEE Transactions on Magnetics*, vol 49, no. 7, July 2013, pp. 4261-4264.
55. M. Darques, J. De La Torre Medina, L. Piraux, L. Cagnon, and I. Huynen. Microwave circulator based on ferromagnetic nanowires in an alumina template, *Nanotechnology*, vo. 21, no. 14, April 2010, pp. 145208.1-4.
56. M. Darques, J. Spiegel, J. De la Torre Medina, I. Huynen, L. Piraux. Ferromagnetic nanowire-loaded membranes for microwave electronics, *Journal of Magnetism and Magnetic Materials (invited paper)*, vol. 321, no. 14, July II, 2009, pp. 2055-2065.

How to cite this article: Williams K., B. Hoskins, R. Lee, G. Masato, and T. Woollings (2016), A regime analysis of Atlantic winter jet variability applied to evaluate HadGEM3-GC2, *Q.J.R. Meteorol. Soc.*, 2017;00:1–6.